Fatigue Behavior of a Fe-Mn-Si Shape Memory Alloy used for Prestressed Strengthening

E. Ghafoori[1,2], E. Hosseini[1,3], C. Leinenbach[1], J. Michels[4], M. Motavalli[1,5]

[1] Empa, Swiss Federal Laboratories for Material Science and Technology, Überlandstrasse 129, CH-8600 Dübendorf, Switzerland

[2] Swinburne University of Technology, VIC 3122 Hawthorn, Melbourne, Australia

[3] Inspire Centre for Mechanical Integrity, c/o Empa, CH-8600 Dübendorf, Switzerland

[4] re-fer AG, Oelistrasse 6, CH-6440 Brunnen, Switzerland

[5] University of Tehran, 16th Azar Street, Tehran, Iran

Abstract

Cyclic deformation and fatigue behavior of an iron-based shape memory alloy (Fe-SMA) Fe-17Mn-5Si-10Cr-4Ni-1(V,C) were studied. In the first step, cyclic tensile tests were performed to characterize the material's mechanical properties in tension (elongation at break, yield, and tensile strength) as well as the recovery behavior of the alloy. Furthermore, the effect of strain rate on the cyclic loading tests was investigated. It was observed that the strain rate has a clear influence on the stress-strain behavior of the alloy. In the second step, the fatigue behavior of the alloy after pre-straining and thermal activation under strain-controlled conditions was evaluated. While the stiffness of the alloy remained almost constant during high-cycle fatigue loading, a decrease in the recovery stress was observed, which should be taken into account in design assessments. The loss in the recovery stress was assumed to be mainly a result of a transformation-induced relaxation (TIR) under cyclic loading. Furthermore, this study examines the applicability of a constant life diagram (CLD) model to determine the fatigue limit of the alloy for different stress ratios (R). The existing results of the fatigue tests showed full

consistency with the proposed fatigue design criterion. A formulation based on the CLD model was proposed for a safe design of the alloy as a structural pre-stressing element under a high-cycle fatigue loading regime.

Keywords: Shape memory alloy (SMA), Fe-Mn-Si SMA, high-cycle fatigue design, fatigue failure criteria, prestressed strengthening, phase transformation.

1. Introduction

Shape memory alloys (SMAs) are materials that have the capability to recover their shape (after they have been deformed at a certain characteristic temperature) by a subsequent heating and cooling process. Most of the existing studies on SMA materials have been conducted on Ni-Ti alloys (also known as Nitinol). Ni-Ti SMAs are already being used for various applications such as medical instruments, aerospace devices, and small mechanical systems. However, the application of the Ni-Ti SMAs for large civil structures is limited because of the high cost of these alloys. As an alternative, Fe-Mn-Si based SMAs have gained much attention because of their relatively low material production cost (compared to Nitinol), good shape memory behavior, and outstanding mechanical properties. Because of these favorable properties, Fe-Mn-Si SMAs are being considered for mechanical engineering applications (such as coupling and tightening systems [1]) and civil structures (for active control [2], damping [3], and pre-stressing elements [4]).

In general, the shape memory effect (SME) in Fe-Mn-Si alloys (also called iron-based or Fe-SMAs) is a result of a stress-induced phase transformation from a parent γ-austenite (fcc – face-centered cubic) phase to an ε-martensite (hcp – hexagonal close-packed) phase at ambient temperatures and its reverse phase transformation (ε-martensite to γ-austenite) upon heating at high temperatures [5]. When the deformation of a Fe-SMA member is constrained during the

reverse phase transformation, the alloy's attempt to revert back to its original shape is not possible, and hence a recovery stress is generated.

One of the most important applications of Fe-Mn-Si SMAs is to use their recovery stress for pre-stressing of structural elements such as concrete and metallic beams and plates. There have been many studies on the utilization of SMAs for pre-stressed confinement of concrete girders [6], concrete columns [7], and steel tensile members [8]. Recently, a novel Fe-17Mn-5Si-10Cr-4Ni-1(V,C) SMA has been developed by some of the authors of the present study at Empa [9-12]. The alloy shows high strength, ductility and recovery stress which make it suitable for civil and mechanical engineering applications [2, 13]. The Fe-17Mn-5Si-10Cr-4Ni-1(V,C) SMA can be manufactured by a standard melting and casting process under atmospheric conditions without thermomechanical training, which makes the large-scale production of the alloy (for civil engineering applications) feasible and hence more cost-effective. Studies on the recovery stress [10], phase transformation [4], creep and stress relaxation [14], and electrochemical and corrosion behavior [15] of the Fe-17Mn-5Si-10Cr-4Ni-1(V,C) SMA indicate a good potential for the alloy as a pre-stressing member for structural engineering applications. Composite pre-stressed members have already been proven to be very effective in increasing the performance of concrete [16, 17] and metallic [18-20] structural engineering elements. Nevertheless, Fe-SMA members can be pre-stressed much more easily than the composite members due to not needing heavy equipment such as hydraulic jacks and complicated anchorage techniques. Therefore, they have a great potential to substantially decrease the work and cost of the whole retrofitting process.

Although there are several studies on the recovery stress and phase transformation of Fe-Mn-Si SMAs, the cyclic and fatigue behaviors of the alloy have not yet been fully investigated. Sawaguchi et al. [3, 21] have studied the low cycle fatigue (LCF) of the alloy but with a focus on its seismic damping and vibration mitigation capabilities. Koster et al. [22] have recently conducted a series of fatigue tests on Fe-17Mn-5Si-10Cr-4Ni-1(V,C) SMA strips; the tests

were performed on non-activated SMA strips under stress-controlled cyclic loading conditions. It has been found that cyclic hardening dominates the LCF regime and fatigue crack initiation occurs as a result of local plastic strain accumulation in the alloy microstructure. Furthermore, it has been concluded that the endurance limit of the alloy is higher than the expected stress ranges for the SMA after activation in pre-stressing applications. Despite this conclusion, the tests in [22] have been performed on non-activated SMA strips and under stress-controlled conditions. However, when a SMA member is used as a pre-stressing element in civil and mechanical engineering structures, it encounters the following conditions - (i) fatigue loading is applied after the activation of the SMA member and (ii) loadings are applied to the SMA member almost always under a strain-controlled condition. The reason for the latter is that the application of the SMA strip has a negligible effect on the stiffness of large civil structures within the service load range [19, 20, 23, 24].

The alloy used in this study is aimed at being used as an external end-anchored or bonded strip for structural strengthening of various civil and mechanical engineering structures, including the existing reinforced concrete (RC) and metallic structures. Therefore, in this study, tests are initially performed to characterize the tensile mechanical and SME properties (e.g., stress recovery and cyclic deformation behavior) of the Fe-17Mn-5Si-10Cr-4Ni-1(V,C) SMA material. Afterwards, the behavior of the pre-stressed (activated) SMA strips subjected to high-cycle fatigue loading is investigated. Finally, a constant life diagram (CLD) model is presented. The CLD approach is particularly useful in designing alloys for high-cycle fatigue loadings after pre-stressing (activation). Such investigations are necessary in order to incorporate fatigue behavior in the structural design.

Note that when discussing fatigue of SMA materials, many parameters can be critical and discussed, for example, change of transformation temperatures, reduction or loss of shape memory, loss of pseudo elasticity or damping capacity [25]. The present work mainly focuses on the change of recovery stress of the Fe-SMA material during high-cycle fatigue loading

regime and also suggests a design criterion to estimate the fatigue limit of the alloy at different stress ratios. The results of this study can be helpful for high-cycle fatigue design of the alloy in civil and mechanical engineering applications. A thorough correlation between the (quasi-)static loading, cyclic loading and low-temperature creep, respectively, and the resulting microstructural changes studied by scanning electron microscopy (SEM), X-ray diffraction (XRD) and electron backscattering diffraction (EBSD) methods can be found in earlier works conducted by some of the present authors [11, 14, 22].

2. General behavior of Fe-Mn-Si SMAs as structural pre-stressing elements

In Fe-SMAs, the austenite phase is stable at the room temperature in a zero stress condition. Figures 1.a and 1.b illustrate the stress-strain and stress-temperature behaviors of the Fe-SMA during the pre-straining and activation process. Figure 1.c shows a schematic view of the application of SMA strips to strengthen an existing structural member subjected to cyclic loading. Different paths in the stress-strain and stress-temperature diagrams in Figs. 1.a and 1.b are correlated to their equivalent application steps in the real-time strengthening process depicted in Fig. 1.c.

In the first step, the alloy is pre-strained to ε_{pre} at room temperature T_0 (see path 1 in Fig. 1.a and Fig. 1.c.i) and then unloaded to zero stress (see path 2 in Fig. 1.a and Fig. 1.c.ii). The loading process (path 1) results in a permanent strain, ε_r, which is mainly due to a forward transformation from the γ-austenite phase to the ε-martensite phase as well as plasticity. The nonlinearity in the unloading curve (path 2) demonstrates some pseudoelasticity (i.e., superelasticity) characteristic of the alloy [11]. Paths 1 and 2 shown in Fig. 1.b at a constant room temperature T_0 correspond to the loading and unloading processes, respectively. In Fig. 1, T_0, and T_h refer to the room temperature, and the maximum heating temperature, respectively.

In the next step, the Fe-SMA element is heated up to T_h (see path 3 in Fig. 1.b and Fig. 1.c.iii) and then cooled down to the room temperature T_0 (see path 4 in Fig. 1.b and Fig. 1.c.iv), while keeping the strain constant at ε_r. The strain in the Fe-SMA is kept constant in order to simulate the behavior of the Fe-SMA elements when they are applied to stiff civil or mechanical structures. The Fe-SMA elements can be attached to metallic or concrete structures in different ways, for example, using mechanical fasteners such as nails or bolts [8] or bonded joints. In Fig. 1.c.iii, it is assumed that the Fe-SMA element is fixed at its both ends to the parent structure using mechanical fasteners. In such conditions, the strain recovery is hindered (by the stiffness of the parent structure) in order to develop a tensile stress in the Fe-SMA member, which then induces a compressive stress in the parent structure. This compressive stress is often beneficial and can result in an increased yield and ultimate load capacity of the parent structure as well as an improved fatigue performance. Note that the assumption of the constant strain at ε_r in this study means that the parent structure has an infinitely large stiffness (i.e., rigid body assumption). However, in reality, parent structures deform when the Fe-SMA element is pre-stressed, which results in a slight decrease in the strain along the Fe-SMA member. The evolution of the recovery stress in the Fe-SMA members under an elastic restraint condition with different compliances have been discussed in [26]. In the next step, an external load is applied to the retrofitted structure, as shown in Fig. 1.c.v, which results in an increase in the stress in the Fe-SMA member (see Path 5 in Figs. 1.a and 1.b).

As can be seen from the path 3 in Fig. 1.b, the stress in the Fe-SMA element drops slightly and becomes negative during the early stages of the heating process, indicating that the thermal expansion effect (TEE) initially dominates the SME. At higher temperatures, however, the martensite to austenite transformation accelerates and as a result, the SME dominates and suppresses the TEE, and hence a tensile stress is developed in the SMA. Note that during the heating step (path 3 in Fig. 1.b), the TEE tends to decrease the stress in the SMA. However, during the cooling process (see path 4 in Fig. 1.b), the effect of the thermal expansion is re-

covered by the thermal contraction of the member and the tensile stress development in the SMA is enhanced. During the cooling process, when the recovery stress exceeds the threshold stress for the martensitic forward transformation, a non-linear behavior is observed in the stress-temperature diagram. The formation of new martensite as well as a pronounced relaxation at larger stress levels tends to decrease the final recovery stress. Note that the shape of paths 3 and 4 is dependent on the heating and the cooling rates.

3. Test set-up, materials, and methods

3.1. Test set-up and specimens

A servo-hydraulic uniaxial testing machine, as shown in Fig. 2.a, was used for the tensile and fatigue loading experiments in this study. A clip-on high temperature axial extensometer with a gauge length of 15 mm was used to measure and control the strain during the tests. In order to prevent excessive heating of the extensometer, ceramic extension rods were used between the induction heating coil and the extensometer. An activation thermal cycle was applied using induction heating and an air cooling system based on the feedback from a spot-welded thermocouple at the center of the specimen. All the dog bone specimens (see Fig. 2.b) were manufactured longitudinal to the rolling direction of the SMA strips.

3.2. Material characterization (as-received state without activation)

The Fe-17Mn-5Si-10Cr-4Ni-1(V,C) (mass%) alloy was fabricated into strips (as explained in [4]) 1.5 mm thick and 100 mm wide. The initial billets from the melting plant were hot-rolled in several steps at elevated temperatures greater than 1000 °C to a strip with a thickness of about 3 mm and a width of 150 mm. Subsequently, cold-rolling was performed to obtain the final thickness of 1.5 mm. Strips of 25 mm width were cut away from both sides in order to

obtain a final width of 100 mm. Eventually, the material was pickled and the surface was grinded.

In order to investigate the microstructure of the as-received alloy, the SEM using a Hitachi S-3700N instrument as well as the XRD using a Bruker D8 instrument (radiation etc.) were conducted. The SEM samples were etched with a Kalling 2 etching solution. Figure 3a shows the results of the SEM tests on the SMA in a back-scattered electron (BSE) mode. The alloy is polycrystalline and the microstructure is characterized by an average grain size of approximately 11 μm. Figure 3a also shows white spots (with sizes < $1\,\mu m$), which are supposed to be carbide precipitates. Figure 3b shows the XRD spectrum of the as-received alloy. Only peaks that can be referred to the austenite phase are visible. However, Figure 3.a shows that some grains contain large bands, which are twins, while many grains contain very fine bands. With regard to the previous microstructural characterization of the alloy by some of the present authors [14, 22] as well as other published work on similar alloys [25, 27, 28], those bands are assumed to be ε-martensite. As those bands are usually very thin, they might be too small to be clearly detected by the XRD.

Tensile tests were conducted to characterize the mechanical properties of the alloy (limit of proportionality, yield, and tensile strength and elongation). In addition to the standard tensile test, an incremental tensile test with repeated loading and unloading was conducted. In this test, the sample was loaded to a total strain of 1 % (in the extensometer gauge length) in the first step, and then unloaded to 0.5 kN. In the subsequent steps, the same procedure was repeated with an increase of 1 % in the total strain in each step. The loading of the specimens was performed under a strain-controlled condition with a constant strain rate of 0.15 % s^{-1}. Because of the measurement limit of the extensometer, for strains larger than 10 %, a machine cross-head displacement rate of 0.075 mm s^{-1} which is approximately equivalent to the gauge length strain rate of 0.15 % s^{-1} was adopted.

Figure 4.a shows the uniaxial deformation response of the SMA at room temperature up to 10 % strain. Table 1 presents the values for the standard 0.01 % and 0.2 % yield strength of the material. Previously, it was found by some of the present authors that $\sigma_{y,0.2}$ does not represent the exact stress where the stress-strain curve begins to show a non-linear behavior [11]. This is because the non-linear behavior starts much earlier than $\sigma_{y,0.2}$ (see Fig. 4.a), which phenomenon has been attributed to the phase transformation from austenite to martensite [11]. Therefore, in this study, $\sigma_{y,0.01}$, which refers to 0.01 % of the non-linear strain was assumed to be the limit of proportionality. An ultimate tensile strength and an initial Young's modulus of approximately 1015 MPa and 173 GPa, respectively, were determined for the SMA used in this study. When compared to the values reported in [11], the ultimate tensile strength of the alloy is slightly larger and the Young's modulus is lower than that reported in [11] (i.e., 993 MPa and 200 GPa, respectively).

Furthermore, Fig. 4.b compares the stress-strain behavior under uniaxial loading condition with (red curve) and without (black curve) intermediate unloading. Hysteresis loops for different strain levels can be observed for the incremental tensile test. From this figure, it can be understood that the unloading curves do not follow the Hook's law (i.e., a linear line), thus allowing us to decipher that the material is pseudo-elastic. The general stress-strain behavior from the incremental tensile test is very similar to that of the as-received alloy. This could imply that the hysteresis loop between the loading and unloading stress-strain curves is mainly caused by the pseudo-elasticity of the alloy rather than by irreversible plasticity. A similar material behavior has been reported in [22].

3.3. Test procedure for activation and cyclic/fatigue testing

When the SMA elements are used as pre-stressing elements in a structure (e.g., bridges, buildings etc.), the whole structure is often subjected to external cyclic loading (due to traffic, tem-

perature changes, wind etc.). This applies an additional cyclic load on the activated SMA. Previous studies by some of the present authors have shown that unlike traditional pre-stressing steels, pre-stressed SMA members do not show a linear elastic behavior in the first loading step [10]. Figure 5 depicts the stress-strain behavior of the activated SMA under a strain-controlled cyclic loading condition (see Fig. 1.c.). The thermo-mechanical processes related to paths 1 to 4 in Fig. 5 have already been discussed in Fig. 1.

As mentioned earlier, the stress in the Fe-SMA element drops slightly during the early stages of the heating process (because of the domination by TEE). Therefore, for the tests performed in this study, in order to avoid the development of a compressive stress during the activation process (i.e., prevention of buckling), the tensile stress was unloaded to a small non-zero value of σ_0 = 50 MPa instead of a full unloading (see the end of path 2 in Fig. 5).

In Fig. 5, the red circle represents the initial recovery stress, σ_r, while σ_r^{15m} represents the reduced recovery stress after 15 min of holding the specimen under the strain-controlled conditions at room temperature. The waiting time of 15 min has been chosen based on a previous report [14], which showed that a major part of the stress relaxation in this type of alloy occurs in the first few minutes after activation. Furthermore, Fig. 5 shows paths 5 and 6 that represent the first additional loading and unloading cycles, respectively (as shown in Figure 1.c.v). σ_{max} and σ_{min} in Fig. 5 refer to the maximum and minimum stresses in the first cycle. The recovery stress is reduced from σ_r^{15m} to σ_{min} after the first loading and unloading. The two important questions here are the influence of the strain rate and subsequent cyclic loading on the maximum stress, σ_{max}, and minimum stress, σ_{min} (the new recovery stress). The answers to these two questions will be provided and discussed in the following sections.

3.4. Test parameters

In this study, a total of five samples were activated and then subjected to cyclic loading. Before activation, all the samples were pre-strained to 2 % and then unloaded to $\sigma_0 =$ 50 MPa. The pre-strain level was chosen based on a previous study [10], which showed that the optimum pre-strain level is 2 %, and pre-strain levels larger than this value do not result in a significant increase in the final recovery stress. The residual strain (see Fig. 5) for all the samples was about ε_r = 1.3 %. The specimens were then heated up to 160 °C and cooled down to the room temperature (25.5 °C) while maintaining a constant strain in the 15 mm extensometer gauge length. The heating and cooling rates during activation were controlled at 2 °C/min. After 15 min (see σ_r^{15m} in Fig. 5), additional cyclic loads were applied to the samples.

Specimens C1 and C2 were subjected to only 10 cyclic loads at a strain range of $\Delta\varepsilon_0$ = 0.07 %. In order to study the effect of frequency (strain rate) on the cyclic behavior of the specimens, C1 and C2 were subjected to two different loading frequencies of 0.002 Hz ($\dot{\varepsilon} = 2.8\times10^{-4}$ % s^{-1}) and 10 Hz ($\dot{\varepsilon} = 1.4$ % s^{-1}). The specimens were then subjected to an increasing tensile load until failure. Note that for all the specimens in this study, the initial pre-straining and the final loading were performed at a strain rate of $\dot{\varepsilon} = 0.15$ % s^{-1}. Note that the final failure tests for all of the samples in this study were performed in a quasi-static manner with a strain rate of 0.15 % s^{-1} up to 10% strain. However, in order to prevent damaging the extensometer for strains larger than 10 %, the extensometer was removed and a cross-head displacement of 0.075 mm s^{-1} was used until failure. Table 2 presents the details of each test specimen, applied cyclic strain range, and the important test results. N_l in this table denotes the number of applied cyclic loads prior to the final tensile loading.

Similar to specimens C1 and C2, specimens F1, F2, and F3 were first activated but then subjected to 2×10^6 cycles with strain ranges of $\Delta\varepsilon_0$ = 0.07 %, 0.035 %, and 0.105 %, respectively. It is believed that the selected strain ranges of 0.035 % and 0.07 % represent the ranges of service loads that are often applied to members in steel [8, 29] and concrete [10] structures,

respectively. The corresponding stress levels and ranges are listed in Table 2. The strain range of 0.105 % is assumed to be larger than the expected service loads on SMA strips for most applications; however, its employment provides a useful parametric evaluation in this investigation. The loading frequency was 10 Hz for all the fatigue tests.

4. Results and discussion

4.1. Cyclic tests on specimens C1 and C2

4.1.1. Generation of recovery stress during the activation process

Figure 6 presents the evolution of the stress in C1 as a function of the strain (Fig. 6.a), time (Fig. 6.b), and temperature (Fig. 6.c). In Fig. 6, the black, blue, green, and red curves refer to the pre-straining, unloading, heating-up, and cooling-down processes, respectively. As expected, the stress slightly drops in the early stages of the heating process (see green curve in Fig. 6.c) due to the TEE. However, the SME dominates quickly after and the stress increases for temperatures greater than 35 °C. This behavior suggests that the transformation of ε-martensite into γ-austenite begins at or very close to the room temperature, and the SME dominates the TEE. The range of austenite start temperature, A_s, obtained in this test is clearly smaller than the A_s temperature of 103 °C [10], which was obtained using differential scanning calorimetry (DSC). The difference might be attributed to the different characteristics of the stress/strain- and thermally-induced phase transformation processes.

During the cooling process (red curve in Fig. 6.c), because of the thermal contraction, the recovery stress further increases. It is to be noted that the stress increase in the heating process is because of the SME. However, the stress increase in the cooling process is due to thermal contraction. Some extent of the forward phase transformation (γ-austenite to ε-martensite) [26] as well as a pronounced relaxation effect are also expected at a higher recovery stress,

which would result in reducing the final recovery stress. Note that the shape of the curves in Fig. 6.c (i.e., thermo-mechanical behavior of the alloy) depends on the heating and the cooling rates. In this study, the heating and the cooling rates were controlled to be 2 °C/min.

4.1.2. Early stage stress behavior

The specimen C1 was pre-strained to 2 % and then unloaded as explained earlier. A recovery stress of σ_r = 372 MPa was achieved after cooling to the room temperature. The recovery stress was decreased to σ_r^{15m} = 364 MPa within the next 15 min under the strain-controlled condition. Table 2 lists the recovery stress values for all the five specimens just after activation and after a 15 min hold time. The stress relaxation during this 15 min holding time ranged from 8 to 14 MPa in different specimens. Stress relaxation is actually a direct consequence of the creep; the results of the creep tests in [14] have shown that the creep strains measured for this alloy are an order of magnitude larger than those reported for high strength steels. This behavior was justified in [14] on the basis of the formation of stress induced martensite from austenite under mechanical loading. The martensite plates are formed gradually at stacking faults through dislocation loops on the layers of the fcc lattice [14]. This is a time-dependent process and is believed to be the main source of the pronounced relaxation in this alloy. Interestingly, it has been observed that unlike in many other metals, the stress relaxation in this alloy is more pronounced at lower temperatures [14]. This behavior has then been explained by the authors to be a result of the γ to ε phase transformation, which is more pronounced at lower temperatures. Therefore, it can be expected that cyclic tests at lower temperatures result in a more pronounced decrease in the recovery stress of the alloy. Note that the microstructural changes and the phase identification during cycling loading has been ana-

lyzed using the XRD and the EBSD measurements in an earlier work by some of the present authors [22].

After 15 min of waiting, the specimen C1 was subjected to ten slow cyclic loadings under strain-controlled conditions with $\Delta\varepsilon_0 = 0.07$ % and a strain rate of 2.8×10^{-4} % s^{-1} (0.002 Hz). The stress-strain behavior during pre-straining, unloading, activation, ten cyclic loadings, and the final failure test is shown in Fig. 7.a. Figure 7.b depicts the details of the stress-strain behavior at different numbers of cycles (N = 1, 3, 6, and 10). It can be observed that the SMA shows a non-linear (inelastic) behavior in the first load cycle and therefore the recovery stress is decreased from 364 MPa to 312 MPa. The reduction in the recovery stress in the first cycle is believed to be due to the austenite to martensite forward phase transformation [11]. For the cycles after the first cycle (N > 1), the SMA shows an almost linear elastic behavior with an apparent Young's modulus of 175.6 GPa, which is very similar to that of the as-received material (173 GPa as shown in Fig. 4.a).

Figure 7.b also presents the results of the specimen C2 that was tested in the same way as specimen C1, but with a larger strain rate of 1.4 % s^{-1} (10 Hz). The aim of these two tests is to better understand the effect of strain rate on the stress-strain behavior of the alloy under cyclic loading conditions. It can be seen from Fig. 7.b that both the maximum and minimum stresses in the first cycles increase with an increase in the strain rate. Furthermore, Fig. 7.c depicts the evolution of σ_{max} and σ_{min} versus the number of cycles. Note that the minimum stress, σ_{min}, is basically the remaining recovery stress, σ_r, after each cycle.

The maximum stresses for C1 and C2 in the first cycle are 434 MPa and 467 MPa, respectively (see Table 2). Similarly, the minimum stresses for C1 and C2 in the first cycle are 312 MPa and 344 MPa, respectively. Although the initial recovery stresses for both specimens are identical, the maximum stress, σ_{max}, in the first cycle for specimen C1 is 33 MPa less than that for specimen C2. This indicates that a pronounced relaxation occurs during the loading at a lower

strain rate (for specimen C1). A possible explanation is the above mentioned low-temperature creep behavior of the alloy that has been explained by the time-dependent γ→ε transformation [14]. Tensile tests with different loading rates showed that the creep strain significantly decreases if the loading rate is decreased, indicating that creep occurs already during slow loading [14]. During the strain-controlled cyclic tests, the time-dependent γ→ε transformation is not completed at the high test frequency of 10 Hz, i.e. the relaxation is less pronounced and the measured maximum and minimum stresses are larger than those at the low test frequency of 0.002 Hz. The stress-strain response during the final loading of the specimens up to 10 % strain is presented in Fig. 7.d. The values of elongation and tensile strength are given in Table 2.

4.2. High-cycle fatigue testing results

Figure 8 presents the results of the high-cycle fatigue tests on specimen F1 with $\Delta\varepsilon_0 = 0.07$ %. A recovery stress of $\sigma_r = 368$ MPa was achieved at first, which then decreased to $\sigma_r^{15m} = 359$ MPa after a 15 min hold time. As explained earlier, the reduction in the recovery stress is mainly due to stress relaxation, which is more pronounced in the first few minutes. Subsequently, the sample was subjected to cyclic loading with $\Delta\varepsilon_0 = 0.07$ % at a frequency of 10 Hz. The enlarged details of the stress-strain behavior at different numbers of cycles (N = 1, 10^2, 10^4, 10^6, 2×10^6) are shown in Fig. 8.a. In the first load cycle, the SMA showed a non-linear behavior and the recovery stress decreased from 359 MPa to 339 MPa (see Table 2). For cycles N = 2 to 2×10^6, the alloy showed an almost linear elastic behavior with a constant Young's modulus; however, the recovery stress decreased gradually to about 284 MPa (a 20 % loss in the recovery stress) after 2×10^6 cycles. In the previous sections, it has been discussed that the phase transformation from γ-austenite to ε-martensite (due to mechanical load-

ing) is a time-dependent process [14]. Such a (delayed) phase transformation is presumed to be the source of relaxation during the 15 min constant strain hold time.

Furthermore, this argument seems to be also valid for the fatigue loading. In [22], it was shown by the EBSD and the XRD measurements that a pronounced $\gamma \rightarrow \varepsilon$ phase transformation occurs at the very early stages of cyclic loading (i.e. the first 10^2 cycles) and becomes less pronounced thereafter. During cyclic loading in the present study, the specimens were subjected to a positive static mean strain in the range between 1.3% and 1.4%. In [14], it was shown that the stress relaxation as a function of time during strain-controlled tensile tests can be described by a simple power law and can reach values of -40 MPa after 1800 s. However, the stress relaxation at times >1800 s was not investigated in that work. At a test frequency of 10 Hz and a maximum number of loading cycles of 2×10^6, the fatigue tests last for 200000 s or 55.5 h and the relaxation will be more pronounced.

This observation is in accordance with the observed increase of the mean strain as a function of the number of loading cycles during stress-controlled fatigue tests [22]. This phenomenon can be considered as a transformation-induced relaxation (TIR) due to cyclic loading.

Figure 8.b depicts the evolution of σ_{max} and σ_{min} versus the number of cycles. It can be seen that the majority of the loss in the recovery stress occurred in the very early stages of fatigue loading (within the first 10^2 to 10^4 cycles, i.e. the first 10 to 1000 s). Furthermore, the stress range due to the application of $\Delta\varepsilon_0 = 0.07$ % seems to remain almost constant even when the number of cycles is changed; however, the mean stress decreased gradually. After applying 2×10^6 load cycles, the specimen was loaded in a quasi-static manner until failure.

Figure 9 depicts the results of fatigue tests on specimen F2 with $\Delta\varepsilon_0 = 0.035$ %. The stress-strain behavior during pre-straining, unloading, fatigue loading, and the final tensile loading up to 10 % strain is shown in Fig. 9.a. Recovery stresses of $\sigma_r = 369$ MPa and $\sigma_r^{15m} = 360$ MPa were achieved. The sample was then subjected to a strain-controlled cyclic loading with $\Delta\varepsilon_0 =$

0.035 % up to $N_l = 2 \times 10^6$ cycles. Figure 9.b illustrates the details of the stress-strain behavior at N = 1, 10^2, 10^4, 10^6, and 2×10^6 cycles. Unlike specimen F1, specimen F2 showed an almost linear stress-strain behavior in the first load cycle and the recovery stress decreased only slightly in the first cycle (from 360 MPa to 358 MPa). The linear behavior can probably be attributed to the small strain range ($\Delta\varepsilon_0 = 0.035$ %) applied to specimen F2, which was half of that for specimen F1. With an increase in the number of cycles, the recovery stress gradually decreased and finally reached 324 MPa (10 % loss in the recovery stress) after 2×10^6 load cycles (see Table 2).

The evolution of σ_{max} and σ_{min} as functions of the number of cycles has been shown in Fig. 9.c, which also includes an inset depicting a log-log plot of the results. This figure shows that the majority of the stress loss (due to the TIR) occurred in the early stages of the cyclic loading. Figure 9.d shows the final tensile loading of specimen F2. It can be seen from this figure that the stress increases sharply up to 2 % strain and then follows the tensile behavior trend of the as-received material. Specimen F2 attained an ultimate tensile strength of 1014 MPa with an elongation of 56.4 %. These values are very similar to those of the as-received material (presented in Table 1) and the specimen F1 (see Table 2).

For specimen F3, recovery stresses of $\sigma_r = 359$ MPa and $\sigma_r^{15m} = 345$ MPa were recorded. The specimen was then subjected to fatigue loading with $\Delta\varepsilon_0 = 0.105$ %. Figure 10.a shows the details of the stress-strain behavior of the specimen at N = 1, 10^2, 10^4, 10^6, and 2×10^6 cycles. It can be seen that because of the relatively large applied strain range of $\Delta\varepsilon_0 = 0.105$ % (three times larger than that for specimen F2), the first load cycle shows a considerable nonlinearity. This resulted in a substantial loss in the recovery stress from 345 MPa to 293 MPa (52 MPa reduction in the first cycle). This behavior indicates that the larger the applied strain, the larger is the loss in the recovery stress in the first cycle. Similar to the specimens described earlier, the recovery stress gradually decreased during cycling to a final value of 170 MPa at $N_l = 2$

$\times 10^6$ cycles. Figure 10.b shows the evolution of the recovery stress (i.e., minimum stress) and the maximum stress versus the number of cycles. Finally, an increasing tensile load was ultimately applied to the specimen. However, an interlock in the testing system resulted in switching off the hydraulic pump, and, therefore the load decreased to zero and the test stopped. Therefore, the tensile strength of this specimen could not be determined. Nonetheless, the general behavior of the material was very similar to that of the other tested specimens.

It is observed that the majority of loss in the recovery stress due to cyclic relaxation occurs during the early stages of cyclic loading. Therefore, in order to have a closer look at the early stages of cyclic loading, the evolution of σ_{max} and σ_{min} in specimens F1, F2, and F3 is shown in Fig. 11.a and Fig. 11.b for 2×10^2 and 2×10^4 cycles, respectively. Furthermore, Figs. 12.a and 12.b depict the relaxation in the recovery stress as a function of the strain range at 2×10^2 and 2×10^4 cycles, respectively. The magnitude of reduction in the recovery stress, $\sigma_{min} - \sigma_r^{15m}$, and the percentage loss as compared to the initial recovery stress, $100 \times \left(\sigma_{min}^{N} - \sigma_r^{15m}\right) / \sigma_r^{15m}$, are shown in Figs. 12.a and 12.b, respectively. The relaxation in the recovery stress increases with an increase in the strain range. This reduction in stress has to be included in design recommendations for this type of material.

5. A CLD model to determine the fatigue strength of the Fe-SMAs at different stress ratios

There are very few and limited studies on the low-cycle [3, 21, 30] and high-cycle [22] fatigue behavior of the Fe-Mn-Si SMAs. There exist, however, many studies on the fatigue behavior and the corresponding microstructural evolution in similar austenitic steels such as austenitic stainless steels [31, 32] or transformation/twinning induced plasticity (TRIP/TWIP) austenite steels with high Mn contents [33-39]. It has been found in the past that the fatigue

behavior of TRIP/TWIP steels is different from that of the conventional steels in terms of the fatigue endurance, which is much higher than the yield stress, due to mechanical twinning effects or phase transformation [34, 38]. However, the fatigue stress limits of some types of austenitic steels have been reported to be similar to those of conventional steels. The fatigue stress limit is a stress level below which no fatigue crack will initiate. The fatigue threshold at a stress ratio of R = -1 is often referred to as the fatigue endurance limit (FEL). Most metals with a body-centered cubic (bcc) crystal structure (e.g., conventional steels) typically have a FEL. However, some metals with fcc crystal structures show a FEL (e.g., TRIP/TWIP austenite steels and austenitic stainless steels), while some others (e.g., aluminum and copper) do not. As the Fe-SMA is an austenitic metal with an fcc crystal structure, it is expected that it has a FEL.

The FEL of steels is often related to their ultimate tensile strength (UTS). The ratio of the FEL/UTS for R = -1 is generally between 0.4 and 0.6 [40, 41]. The FEL has been determined for different types of austenitic stainless steels (e.g., AISI 304, 316L, and 301LN) with UTS ranging from 595 MPa to 1700 MPa, resulting in a FEL/UTS ratio between 0.4 and 0.5 [31, 32, 34]. Hamada et al. [34] performed high-cycle fatigue tests on different types of high-Mn TWIP steels with the UTS ranging from 830 MPa to 963 MPa. They reported a FEL/UTS ratio in the range of 0.42 to 0.48. For both austenitic stainless steels and high-Mn TWIP steels, the FEL has been reported to be often around or higher than the material yield stress, dissimilar to that in conventional steels [40]. The ratio of FEL/UTS obtained for austenitic stainless steels as well as TWIP steels is fully consistent with the range reported for conventional steels.

5.1. Applicability of the CLD approach for Fe-SMA

One of the aims of this study is to examine the applicability of the CLD approach to estimate the fatigue limit of the Fe-SMA under different stress ratios. This is of great importance as Fe-

SMA is often used as a pre-stressing member that is subjected to service loads, resulting in large stress ratios. The CLD methodology takes into account the effects of the mean stress, alternating stress, and material properties to calculate the lifetime of the material in a high-cycle fatigue loading regime [42]. The validity of the CLD approach for conventional steels is generally accepted [40, 43]. The two main input parameters in the CLD approach are the FEL and the UTS. Although the ratio of FEL to the yield stress for Fe-SMA is very different from that for conventional steels, based on the discussions in the previous sub-section, it is expected that the FEL/UTS ratio of Fe-SMA would be within the typical range of that for conventional steels. Therefore, it can also be expected that the CLD approach would be valid for Fe-SMA. In this section, the existing fatigue test results for Fe-SMA from the current and a previous [22] study will be presented using a CLD methodology. The proposed CLD method can help in designing the allowable service stress due to additional service loading after activation of the SMA.

5.2. The proposed CLD model

Cyclic stresses are often sinusoidal, as shown in Fig. 13.a. The mean stress, σ_m, and stress amplitude, σ_a, are given by

$$\sigma_m = \frac{\sigma_{max} + \sigma_{min}}{2} \tag{1.a}$$

$$\sigma_a = \frac{\sigma_{max} - \sigma_{min}}{2} \tag{1.b}$$

where $\sigma_{\max}$ and $\sigma_{\min}$ are the maximum and the minimum stresses, respectively, in the sinusoidal stress pattern. The stress ratio, R, is defined by

$$R = \frac{\sigma_{min}}{\sigma_{max}} \tag{2}$$

Figure 13.b shows a CLD that demonstrates three main stress regions. The middle region bounded by R = 0 and R = ±∞ is for tension-compression stresses, while the right region bounded by R = 1 and R = 0 is for tension-tension stresses. The left region bounded by R = ±∞ and the horizontal axis is for compression-compression stresses. The existing results of fatigue failure tests in the literature [40, 43] on traditional steels show that as the mean stress level increases, fatigue failure occurs at a decreased stress amplitude. Gerber [43] has suggested a parabola for ductile steels, which passes through $\sigma_a = S_e$ and $\sigma_m = S_{ut}$ with a criterion equation, given as follows

$$\frac{\sigma_a}{S_e} + \left(\frac{\sigma_m}{S_{ut}}\right)^2 = 1 \tag{3}$$

where S_e is the FEL and is a function of the material properties and surface preparation, as will be explained later. Figure 13.b shows the Gerber failure criterion. Goodman [40], however, has proposed a linear line through $\sigma_a = S_e$ and $\sigma_m = S_{ut}$ (Eq. (4))

$$\frac{\sigma_a}{S_e} + \frac{\sigma_m}{S_{ut}} = 1 \tag{4}$$

Based on the results of the existing fatigue failure tests in the literature [19, 24, 40, 43], Ghafoori et al. [24] have suggested three different regions in the CLD with different fatigue failure probabilities for ductile steels such as structural mild steels. Figure 13.b. illustrates the level of fatigue failure probability using different markers. The blue area, inside the modified Goodman line in Fig. 13.b, is assumed to be safe against fatigue and has infinite fatigue life. The triangle marker shows the safe zone, in which no macrocracks form under a high-cycle fatigue loading regime. The yellow square marker indicates the risky zone, where macrocracks might form. The red circular marker shows the unsafe region, where there is a high probability of macrocrack formation [24]. As the Fe-SMA shows a very ductile material behavior, it is then expected that the approach suggested in [24] for structural ductile steels (which is based on the Goodman failure criterion) would also be valid for the Fe-SMA mate-

rial. The validity of this assumption will be examined later in this study using the existing fatigue test results on the alloy.

In this study, Eq. (5) is used to estimate the FEL of the Fe-SMA strips for R = -1, which is consistent with the proposed formulation for traditional steels [40].

$$S_e^{'} = 0.45 S_{ut} \qquad S_{ut} \le 1400\,\text{MPa} \tag{5}$$

The prime sign on $S_e^{'}$ in Eq. (5) refers to fatigue tests on rotating-beam specimens with a stress ratio of R = -1. The rotating-beam specimens are prepared very carefully and tested under laboratory conditions. It is not reasonable to assume that the FELs of all structural elements are of the same value as that achieved under laboratory conditions. Marin has proposed various coefficients to quantify the effects of surface condition, loading, temperature, and size (through statistical analysis) [15] on the FEL (Eq. (6))

$$S_e = k_a k_b k_c k_d k_e S_e^{'} \tag{6}$$

where k_a, k_b, k_c, k_d, and k_e are the modification coefficients for surface condition, size, load, temperature, and reliability, respectively. Note that while $S_e^{'}$ is the FEL achieved through the fatigue tests on rotary-beam test specimens, S_e is the endurance limit during the condition of use. A simple procedure to calculate the Marin coefficients for specimens other than rotating-beam specimens can be found elsewhere [19, 23].

In order to examine the validity of the proposed CLD model, the results of the existing fatigue tests on Fe-SMA are compared with the proposed CLD model (see Fig. 14). The circle markers show the results of the fatigue tests previously conducted by some of the present authors [22]. The markers with a red filling indicate the failed specimens while the markers with a green filling denote the specimens that survived after 2×10^6 cycles (run-out specimens). Furthermore, in Fig. 14, the square markers show the results of the present test program. As the tests in this study were performed under a strain-controlled condition and the stress levels de-

creased with an increase in the number of cycles, the initial and final stresses are different and have been denoted by “i” and “f”, respectively, in Fig. 14.

For the Fe-SMA strips, Marin factors of $k_a = 0.72$ (machined/cold-worked), $k_b = 1$ (under axial loading), $k_c = 0.85$, $k_d = 1$ (laboratory temperature), and $k_e = 1$ (50 % reliability) were used. More details on the determination of the Marin factors can be found in [19, 23]. Based on the Eqs. (5) and (6), the FEL of the Fe-SMA strips is calculated as

$$S_e = 0.275\, S_{ut} \tag{7}$$

S_{ut} of the Fe-SMA in [22] has been reported to be 993 MPa, which results in a S_e of 273 Mpa. Once the S_e is calculated, Eqs. (3) and (4) are used to plot the Gerber and Goodman lines, respectively, as shown in Fig. 14.

From Fig. 14, it can be observed that the cyclic stresses located inside the Goodman line (safe zone) survived after 2×10^6 cycles, while the cyclic stresses outside the Gerber parabola (unsafe zone) failed in less than 2×10^6 cycles. The cyclic stresses that lie between the Goodman and Gerber curves (risky zone) could result in fatigue failure or survival. This behavior is very similar to the fatigue behavior of traditional steels, as shown in Fig. 13.b.

From Fig. 14, it can also be seen that for the specimens in the current study (square markers), both the initial and the final stresses were inside the safe region, and, therefore, no fatigue fracture was expected for these specimens. Furthermore, the figure shows that the stress ranges for specimens F1, F2, and F3 decrease only slightly after cyclic loadings. However, the mean stress level decreases considerably. This behavior shows that the decrease in the stiffness of the alloy during high-cycle fatigue is negligible; however, the reduction in the recovery stress has to be taken in account in design. For design purposes, the maximum and the minimum stress levels in the first load cycle can be used.

Based on the available test results, the Goodman criterion seems to be working well as a failure criterion to prevent fatigue cracks in the Fe-SMA strips. Therefore, substitution of Eq. (7) into Eq. (4) results in

$$3.6\sigma_a + \sigma_m \le S_{ut} \qquad \text{for} \quad -1 \le R \le 1 \tag{8}$$

The inequality sign in Eq. (8) is used to show the safe region inside the Goodman line in the first quadrant of the presented CLD ($-1 \le R \le 1$). Using Eqs. (1) and (2), Eq. (8) can be alternatively presented in terms of R and σ_{max} as

$$\sigma_{max} \le \frac{S_{ut}}{2.3 - 1.3R} \qquad \text{for} \quad -1 \le R \le 1 \tag{9}$$

Equations (8) and (9) describe the general fatigue behavior of the Fe-SMA strips. For design purposes, it is recommended to use S_{ut}/n instead of S_{ut}, where n is the safety factor. Note that R in this study refers to the cyclic stress ratio that is experienced by the Fe-SMA member and not the parent structure. Different Fe-SMA products such as strips and bars exist in the market [44]. This study focuses on the fatigue behavior and design of the Fe-SMA strips, however similar approach could be adopted for fatigue design of Fe-SMA bars.

Furthermore, Fig. 14 shows the yield criterion, which is given by

$$\sigma_a + \sigma_m = \sigma_y \tag{10}$$

In Fig. 14, $\sigma_{y,0.01}$ yield line is shown, which indicates that the fatigue limit calculated by Eq. (9) is well above the $\sigma_{y,0.01}$ yield stress of the alloy at different stress ratios. Note that although $\sigma_{y,0.01}$ yield line is inside the predicted fatigue safe region, the $\sigma_{y,0.2}$ yield criterion lies partly outside of the fatigue safe region (determined by Eq. (9)) at lower stress ratios between R=-1 and R=0. Therefore, the $\sigma_{y,0.2}$ yield criterion is not conservative, and, hence not recommended for fatigue design of the alloy.

The Fe-SMA strips are sometimes applied to concrete and steel members [8] using mechanical fasteners such as bolts or rivets. In such cases, there is a need to drill holes in the Fe-SMA strips, which allow stress concentration in the vicinity of the edges of the hole. Stress concentration factors (SCFs) are often used to take into account the effect of such holes or notches for traditional steels. A SCF is defined as the ratio of the maximum stress at the edge of a hole

to the nominal (far-field) stress of the section. The concept of SCF is typically used for cases when the metal is within the elastic linear domain. However, based on Fig. 14, the stresses along the pre-stressed Fe-SMA are larger than the material yield stress. Therefore, there is a need to perform a non-linear finite element analysis (FEA) to estimate the stress state at the edges of the holes. After the SCFs have been determined by the FEA, the fatigue SCF can be calculated by considering a notch-sensitivity factor [45], as explained in [24].

6. Summary

The behavior of a Fe-17Mn-5Si-10Cr-4Ni-1(V,C) SMA subjected to tensile and fatigue loading was studied. A total of five samples were pre-strained, activated, and later subjected to cyclic loading. All the five specimens were pre-strained to 2 %, unloaded, and then activated by heating up to 160 °C. The recovery stress ranged from 359 MPa to 372 MPa, confirming the earlier reported observations regarding the magnitude of the recovery stress. Furthermore, the validity of the CLD approach to determine the fatigue limit of the alloy was examined. The following conclusions were drawn from this study:

1. Cyclic loading was applied with two different strain rates. The larger strain rate resulted in the development of larger stresses in the alloy. Loading with lower strain rates resulted in reduced stress levels which could be because of the stress relaxation that begins in the early stages during the slow loading process. This observation indicates that the magnitude of strain rate has a clear effect on the stress-strain behavior of the Fe-SMA.
2. The selected strain ranges of 0.035 % and 0.07 % for fatigue tests represent the ranges of common stress amplitudes that are often applied to steel and concrete structures, respectively. After 2×10^6 cycles, no material fracture was observed. However, the recovery stress decreased by nearly 10 % and 20 % for the strain ranges of 0.035 % and

0.07 %, respectively. This loss in the recovery stress should be considered in the structural design.

3. As the austenite to martensite phase transformation (caused by mechanical loading) is a time-dependent process, the TIR phenomenon (rather than an irreversible plasticity) was assumed to have reduced the recovery stress during the cyclic loading process. The delayed γ→ε phase transformation is probably the main source of relaxation when the alloy is subjected to strain-controlled cyclic loading. This conclusion is in agreement with the results of the EBSD and the XRD analysis, which have been performed in a previous study by some of the present authors [22]. Furthermore, a greater reduction in the recovery stress was observed with an increase in the strain range.
4. A CLD model was proposed to predict the fatigue limit of the alloy at different stress ratios. The results of the existing tests showed that the Goodman fatigue failure criterion can conservatively predict the fatigue limit of the Fe-SMA strips for $-1 \le R \le 1$. From the experimental and theoretical results, it was concluded that the inequality $\sigma_{max} \le S_{ut} / (2.3 - 1.3R)$ can be used for the safe design of an alloy subjected to a high-cycle fatigue loading regime.
5. Based on the proposed CLD approach, the $\sigma_{y,0.01}$ yield criterion is well below the fatigue limit of the alloy at all stress ratios ($-1 \le R \le 1$). The $\sigma_{y,0.2}$ yield criterion, however, can be above the fatigue limit, particularly, at lower stress ratios of $-1 \le R \le 0$, and, therefore, it is not conservative for fatigue design purposes.
6. After the application of 2×10^6 load cycles, the alloy was subjected to an increasing tensile stress up to failure. It was observed that for all the specimens, the stress-strain curve increased sharply until 2 % strain (initial pre-straining level) and then was similar to the stress-strain curve of the as-received material until failure, independent of the magnitude of the stress relaxation due to prior cyclic loading.

Acknowledgments

The authors would like to acknowledge the contribution of Dr. M. Shahverdi, Dr. C. Czaderski and Dr. B. Weber from the Empa in the process of developing the test plan of this study. Furthermore, the authors would like to thank Dr. A. Arabi-Hashemi from the Empa for performing the SEM tests.

References

1. Maruyama T., Kurita T., Kozaki S., Andou K., Farjami S., Kubo H. Innovation in producing crane rail fishplate using Fe–Mn–Si–Cr based shape memory alloy. Materials Science and Technology, 2008. 24(8): p. 908-912.
2. Janke L., Czaderski C., Motavalli M., Ruth J. Applications of shape memory alloys in civil engineering structures - Overview, limits and new ideas. Materials and Structures/Materiaux et Constructions, 2005. 38(279): p. 578-592.
3. Sawaguchi T., Sahu P., Kikuchi T., Ogawa K., Kajiwara S., Kushibe A., Higashino M., Ogawa T. Vibration mitigation by the reversible fcc/hcp martensitic transformation during cyclic tension–compression loading of an Fe–Mn–Si-based shape memory alloy. Scripta Materialia, 2006. 54(11): p. 1885-1890.
4. Czaderski C., Shahverdi M., Brönnimann R., Leinenbach C., Motavalli M. Feasibility of iron-based shape memory alloy strips for prestressed strengthening of concrete structures. Construction and Building Materials, 2014. 56(0): p. 94-105.
5. Sato A., Chishima E., Soma K., Mori T. Shape memory effect in γ⇄ϵ transformation in Fe-30Mn-1Si alloy single crystals. Acta Metallurgica, 1982. 30(6): p. 1177-1183.
6. Czaderski C., Hahnebach B., Motavalli M. RC beam with variable stiffness and strength. Construction and Building Materials, 2006. 20(9): p. 824-833.
7. Mohd Jani J., Leary M., Subic A., Gibson M.A. A review of shape memory alloy research, applications and opportunities. Materials & Design (1980-2015), 2014. 56: p. 1078-1113.
8. Izadi M.R., Ghafoori E., Hosseini A., Motavalli M., Maalek S., Shahverdi M. Feasibility of iron-based shape memory alloy strips for prestressed strengthening of steel plates, in the fourth International Conference on Smart Monitoring, Assessment and Rehabilitation of Civil Structures (SMAR 2017). 2017: Zurich, Switzerland.
9. Dong Z., Klotz U.E., Leinenbach C., Bergamini A., Czaderski C., Motavalli M. A novel Fe-Mn-Si shape memory alloy with improved shape recovery properties by VC precipitation. Advanced Engineering Materials, 2009. 11(1-2): p. 40-44.
10. Lee W.J., Weber B., Feltrin G., Czaderski C., Motavalli M., Leinenbach C. Stress recovery behaviour of an Fe–Mn–Si–Cr–Ni–VC shape memory alloy used for prestressing. Smart Materials and Structures, IOP Science, 2013. 22: p. 1-9.
11. Lee W.J., Weber B., Feltrin G., Czaderski C., Motavalli M., Leinenbach C. Phase transformation behavior under uniaxial deformation of an Fe–Mn–Si–Cr–Ni–VC shape memory alloy. Materials Science and Engineering: A, 2013. 581: p. 1-7.
12. Leinenbach C., Kramer H., Bernhard C., Eifler D. Thermo-mechanical properties of an Fe-Mn-Si-Cr-Ni-VC shape memory alloy with low transformation temperature. Advanced Engineering Materials, 2012. 14(1-2): p. 62-67.

13. Cladera A., Weber B., Leinenbach C., Czaderski C., Shahverdi M., Motavalli M. Iron-based shape memory alloys for civil engineering structures: An overview. Construction and Building Materials, 2014. 63(0): p. 281-293.
14. Leinenbach C., Lee W.J., Lis A., Arabi-Hashemi A., Cayron C., Weber B. Creep and stress relaxation of a FeMnSi-based shape memory alloy at low temperatures. Materials Science and Engineering A, 2016. 677: p. 106-115.
15. Lee W.J., Partovi-Nia R., Suter T., Leinenbach C. Electrochemical characterization and corrosion behavior of an Fe-Mn-Si shape memory alloy in simulated concrete pore solutions. Materials and Corrosion, 2016. 67(8): p. 839-846.
16. Michels J., Martinelli E., Czaderski C., Motavalli M. Prestressed CFRP strips with gradient anchorage for structural concrete retrofitting: Experiments and numerical modeling. Polymers, 2014. 6(1): p. 114-131.
17. Michels J., Sena-Cruz J., Czaderski C., Motavalli M. Structural strengthening with prestressed CFRP strips with gradient anchorage. Journal of Composites for Construction, 2013. 17(5): p. 651-661.
18. Ghafoori E., Motavalli M. Normal, high and ultra-high modulus CFRP laminates for bonded and un-bonded strengthening of steel beams. Materials and Design, 2015. 67: p. 232–243.
19. Ghafoori E., Motavalli M., Nussbaumer A., Herwig A., Prinz G., Fontana M. Determination of minimum CFRP pre-stress levels for fatigue crack prevention in retrofitted metallic beams. Engineering Structures, 2015. 84: p. 29–41.
20. Ghafoori E., Prinz G.S., Mayor E., Nussbaumer A., Motavalli M., Herwig A., Fontana M. Finite element analysis for fatigue damage reduction in metallic riveted bridges using pre-stressed CFRP plates. Polymers, 2014. 6(4): p. 1096-1118.
21. Sawaguchi T., Nikulin I., Ogawa K., Sekido K., Takamori S., Maruyama T., Chiba Y., Kushibe A., Inoue Y., Tsuzaki K. Designing Fe–Mn–Si alloys with improved low-cycle fatigue lives. Scripta Materialia, 2015. 99: p. 49-52.
22. Koster M., Lee W.J., Schwarzenberger M., Leinenbach C. Cyclic deformation and structural fatigue behavior of an FE–Mn–Si shape memory alloy. Materials Science and Engineering: A, 2015. 637(0): p. 29-39.
23. Ghafoori E., Motavalli M., Nussbaumer A., Herwig A., Prinz G.S., Fontana M. Design criterion for fatigue strengthening of riveted beams in a 120-year-old railway metallic bridge using pre-stressed CFRP plates. Composites Part B: Engineering, 2015. 68: p. 1-13.
24. Ghafoori E., Motavalli M., Zhao X.L., Nussbaumer A., Fontana M. Fatigue design criteria for strengthening metallic beams with bonded CFRP plates. Engineering Structures, 2015. 101: p. 542-557.
25. Hornbogen E. Review Thermo-mechanical fatigue of shape memory alloys. Journal of Materials Science, 2004. 39(2): p. 385-399.
26. Lee W.J., Weber B., Leinenbach C. Recovery stress formation in a restrained Fe–Mn–Si-based shape memory alloy used for prestressing or mechanical joining. Construction and Building Materials, 2015. 95: p. 600-610.
27. Bergeon N., Guenin G., Esnouf C. Microstructural analysis of the stress-induced ε martensite in a Fe–Mn–Si–Cr–Ni shape memory alloy: Part I—calculated description of the microstructure. Materials Science and Engineering: A, 1998. 242(1–2): p. 77-86.
28. Bergeon N., Kajiwara S., Kikuchi T. Atomic force microscope study of stress-induced martensite formation and its reverse transformation in a thermomechanically treated Fe–Mn–Si–Cr–Ni alloy. Acta Materialia, 2000. 48(16): p. 4053-4064.
29. Hosseini A., Ghafoori E., Motavalli M., Nussbaumer A., Zhao X.-L. Mode I Fatigue Crack Arrest in Tensile Steel Members Using Prestressed CFRP Plates. Composite Structures, 2017. DOI: doi.org/10.1016/j.compstruct.2017.06.056.
30. Sawaguchi T., Kikuchi T., Kajiwara S. The pseudoelastic behavior of Fe-Mn-Si-based shape memory alloys containing Nb and C. Smart Materials and Structures, 2005. 14(5): p. S317-S322.

31. http://www.bssa.org.uk/topics.php?article=104. [Accessed on 15 April 2017].
32. Uusitalo J., Karjalainen L.P., Retraint D., Palosaari M. Fatigue properties of steels with ultrasonic attrition treated surface layers, in Materials Science Forum. 2009. p. 239-248.
33. Cheng X., Petrov R., Zhao L., Janssen M. Fatigue crack growth in TRIP steel under positive R-ratios. Engineering Fracture Mechanics, 2008. 75(3-4): p. 739-749.
34. Hamada A.S., Karjalainen L.P., Puustinen J. Fatigue behavior of high-Mn TWIP steels. Materials Science and Engineering A, 2009. 517(1-2): p. 68-77.
35. Niendorf T., Rubitschek F., Maier H.J., Niendorf J., Richard H.A., Frehn A. Fatigue crack growth-Microstructure relationships in a high-manganese austenitic TWIP steel. Materials Science and Engineering A, 2010. 527(9): p. 2412-2417.
36. Nikulin I., Sawaguchi T., Kushibe A., Inoue Y., Otsuka H., Tsuzaki K. Effect of strain amplitude on the low-cycle fatigue behavior of a new Fe-15Mn-10Cr-8Ni-4Si seismic damping alloy. International Journal of Fatigue, 2016. 88: p. 132-141.
37. Nikulin I., Sawaguchi T., Ogawa K., Tsuzaki K. Low-cycle fatigue behavior and microstructural evolution of the Fe- 30Mn-4Si-2Al alloy, in Advanced Materials Research. 2014. p. 944-949.
38. Nikulin I., Sawaguchi T., Tsuzaki K. Effect of alloying composition on low-cycle fatigue properties and microstructure of Fe-30Mn-(6-x)Si-xAl TRIP/TWIP alloys. Materials Science and Engineering A, 2013. 587: p. 192-200.
39. Robertson L.T., Hilditch T.B., Hodgson P.D. The effect of prestrain and bake hardening on the low-cycle fatigue properties of TRIP steel. International Journal of Fatigue, 2008. 30(4): p. 587-594.
40. Budynas R.G., Nisbett J.K. Shigley's Mechanical Engineering Design. 2008, New York: McGraw-Hill.
41. Chapetti M.D., Miyata H., Tagawa T., Miyata T., Fujioka M. Fatigue strength of ultra-fine grained steels. Materials Science and Engineering A, 2004. 381(1-2): p. 331-336.
42. Ghafoori E., Motavalli M. A Retrofit Theory to Prevent Fatigue Crack Initiation in Aging Riveted Bridges Using Carbon Fiber-Reinforced Polymer Materials. Polymers, 2016. 8: p. 308.
43. Klubberg F., Klopfer I., Broeckmann C., Berchtold R., Beiss P. Fatigue testing of materials and components under mean load conditions. Anales de Mecánica de la Fractura, 2011. 1(28): p. 419-424.
44. www.re-fer.eu/en. [accessed on 19 May 2017].
45. Sines G., H.L. W. Metal fatigue. 1969: McGraw-Hill, New York. Copyright 1969 by The McGraw-Hill Companies, Inc.

Figures and Tables

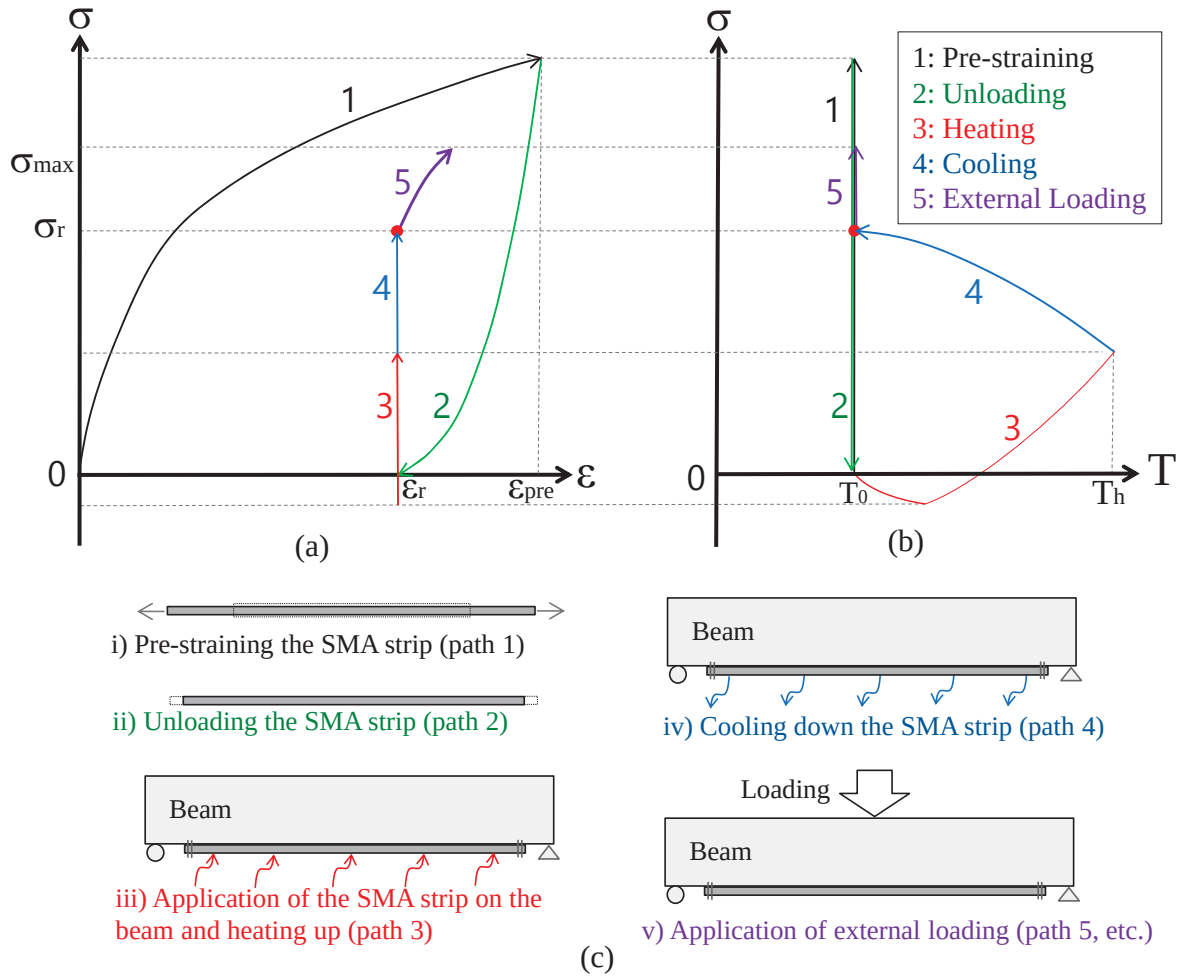

Fig. 1. (a) The stress-strain and (b) stress-temperature behaviors of the Fe-Mn-Si SMA material. (c) Application of SMA strips to strengthen an existing structural member subjected to cyclic loading - Pre-straining (path 1), unloading (path 2), heating (path 3), cooling (path 4), and application of external loading (path 5) processes.

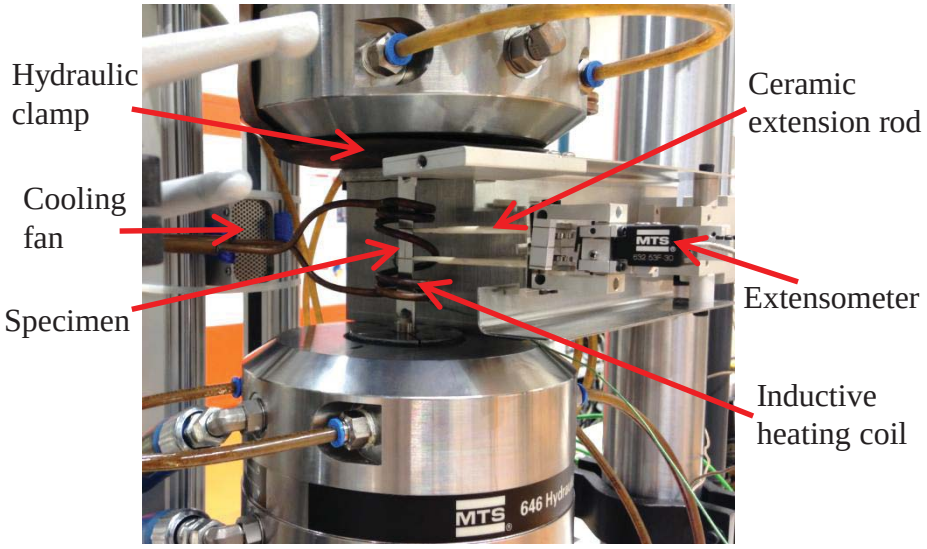

(a)

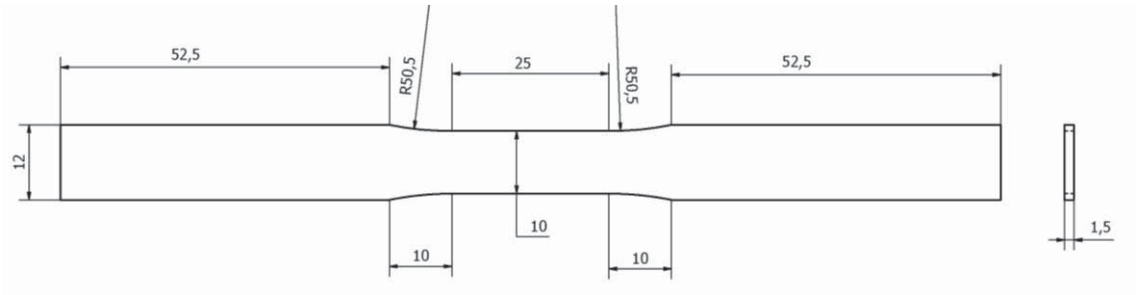

(b)

Fig. 2. (a) Servo-hydraulic uniaxial testing machine with an inductive heating system and (b) the geometry of the dog bone specimens used for the tests (dimensions in mm).

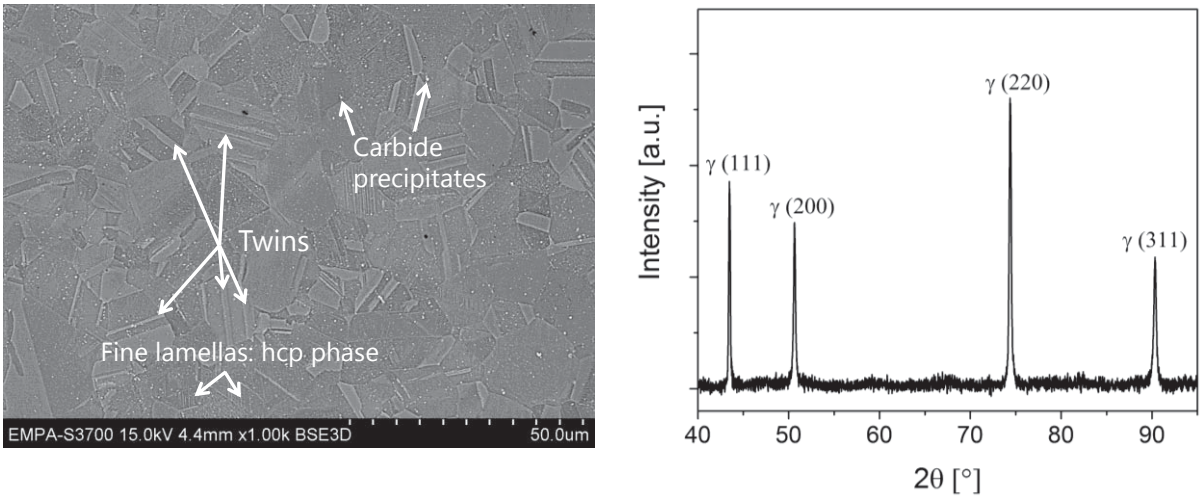

(a) (b)

Fig. 3. Microstructure of the as-received Fe-17Mn-5Si-10Cr-4Ni-1(V,C) SMA. (a) The SEM in the BSE mode shows large twin bands and fine hcp-phase bands. (b) The XRD spectrum of the as-received alloy at room temperature.

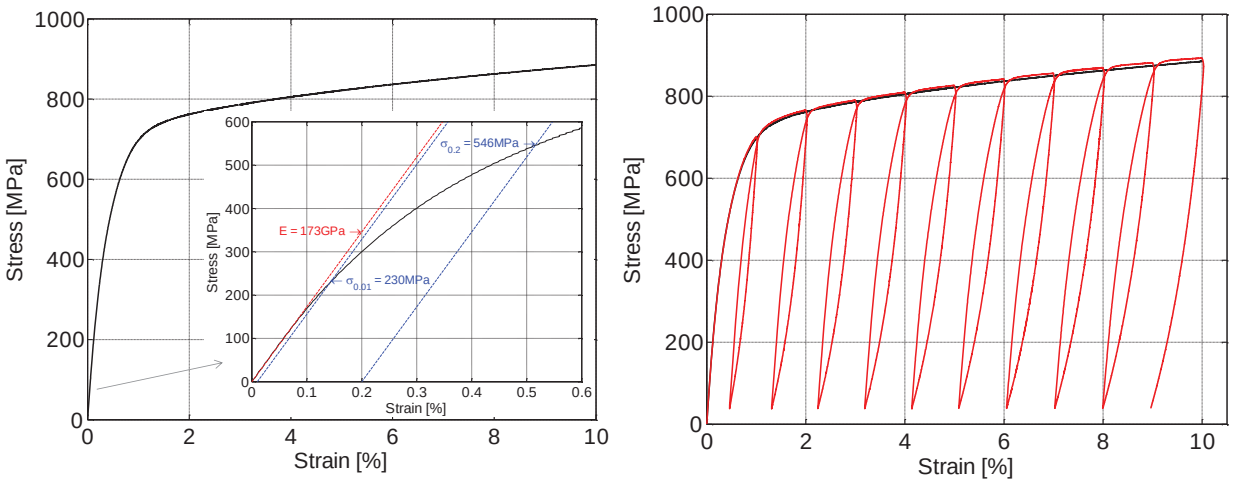

Fig. 4. Uniaxial deformation response of the alloy at room temperature (a) up to 10 % strain and (b) comparison of the alloy stress-strain behavior under uniaxial loading condition with and without intermediate unloading.

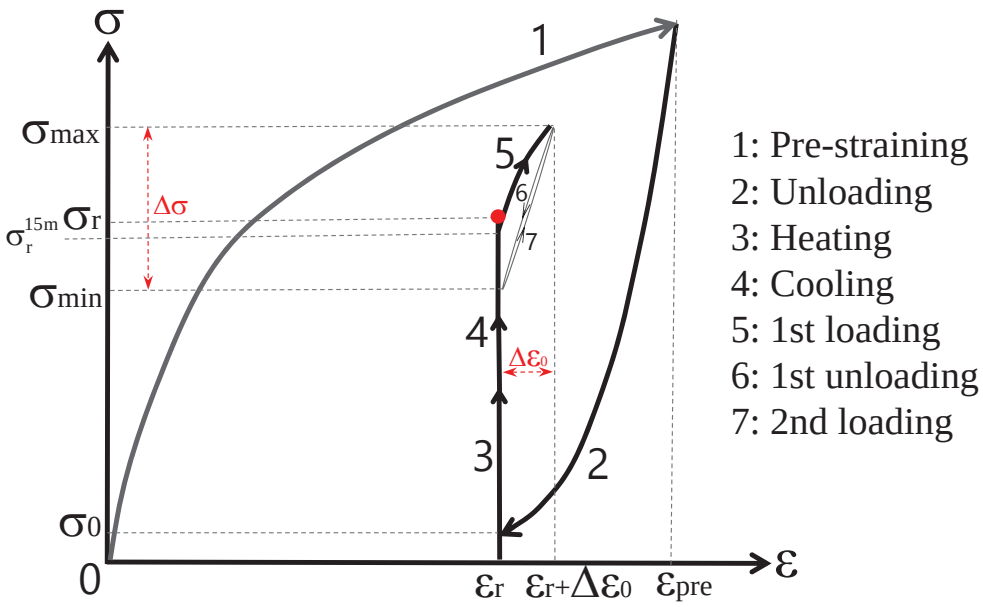

Fig. 5. Stress-strain behavior of the Fe-SMA during the application of cyclic loading (after activation of the SMA) under strain-controlled conditions.

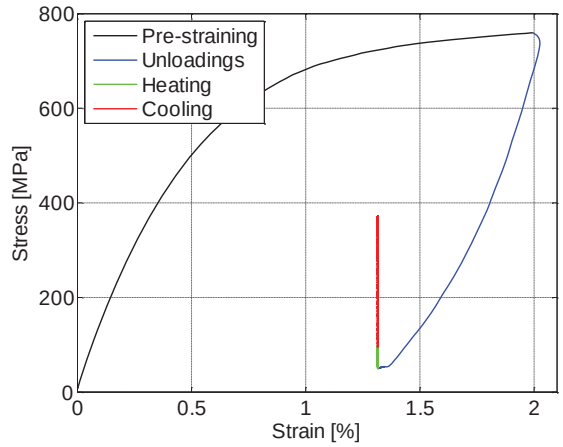

(a)

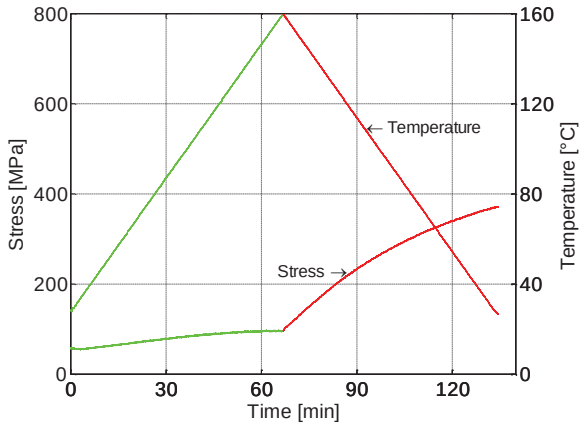

(b)

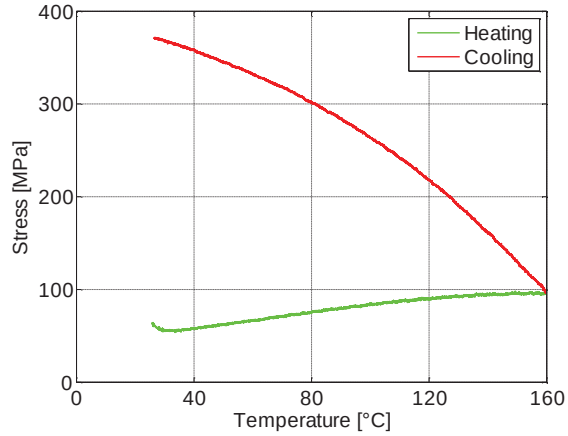

(c)

Fig. 6. Recovery stress of specimen C1 versus (a) strain, (b) time, and (c) temperature. The black, blue, green, and red curves represent the pre-straining, unloading, heating-up, and cooling-down processes, respectively.

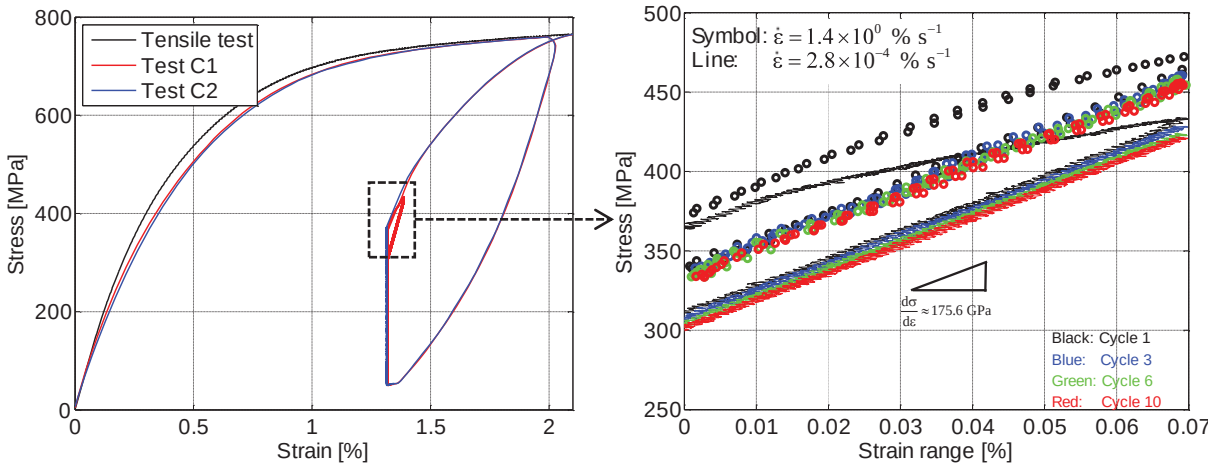

(a) (b)

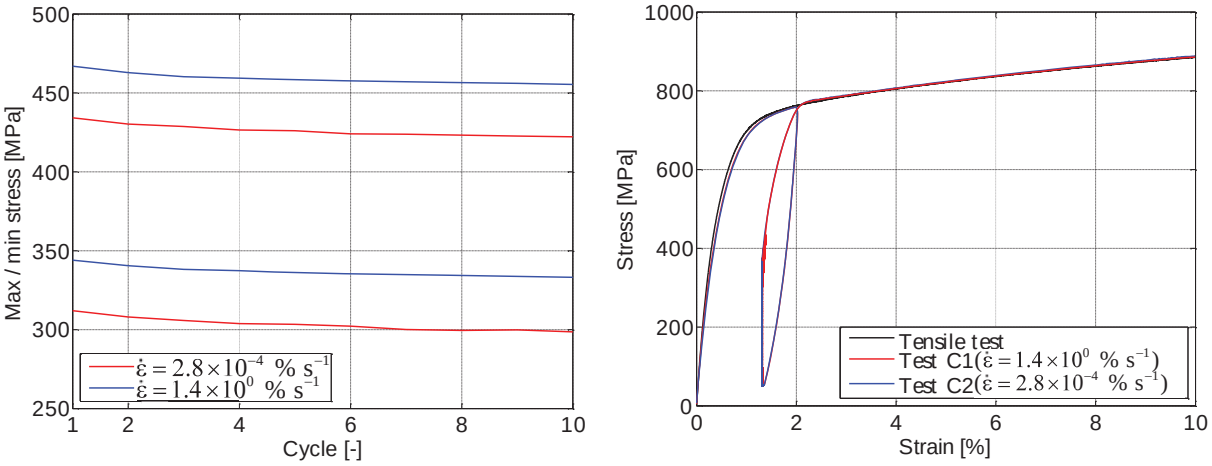

(c) (d)

Fig. 7. Specimens C1 and C2: (a) the stress-strain behavior during pre-straining, unloading, ten loading cycles, and the final failure, (b) the enlarged details of the cyclic behavior of the activated SMA for $\Delta\varepsilon_0 = 0.07$ % at two different strain rates, (c) the evolution of σ_{max} and σ_{min} versus the number of cycles, and (d) the final loading until failure.

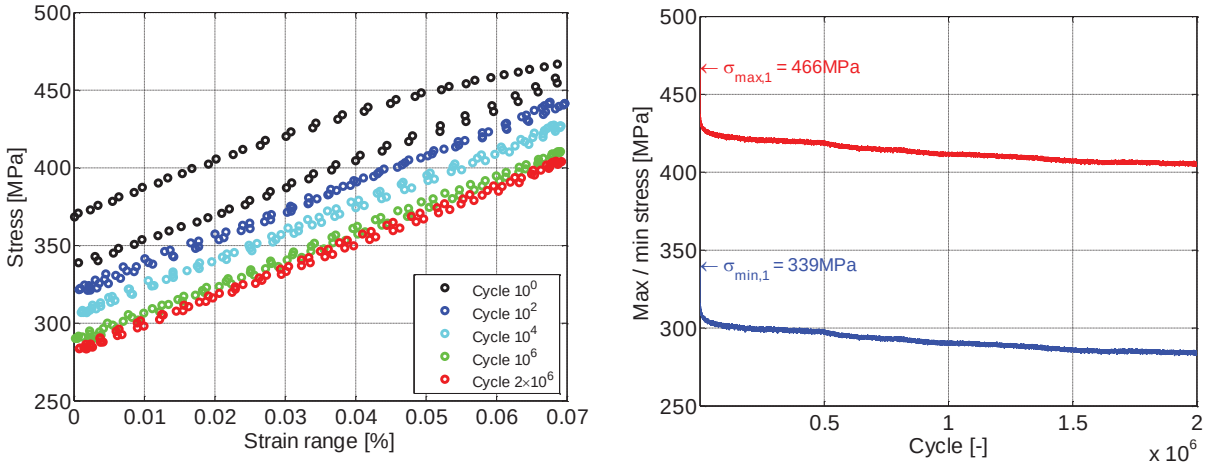

(a) (b)

Fig. 8. Specimen F1: (a) the deformation response of the activated SMA under fatigue loading with $\Delta\varepsilon_0 = 0.07$ % and (b) the evolution of σ_{max} and σ_{min} versus the number of cycles.

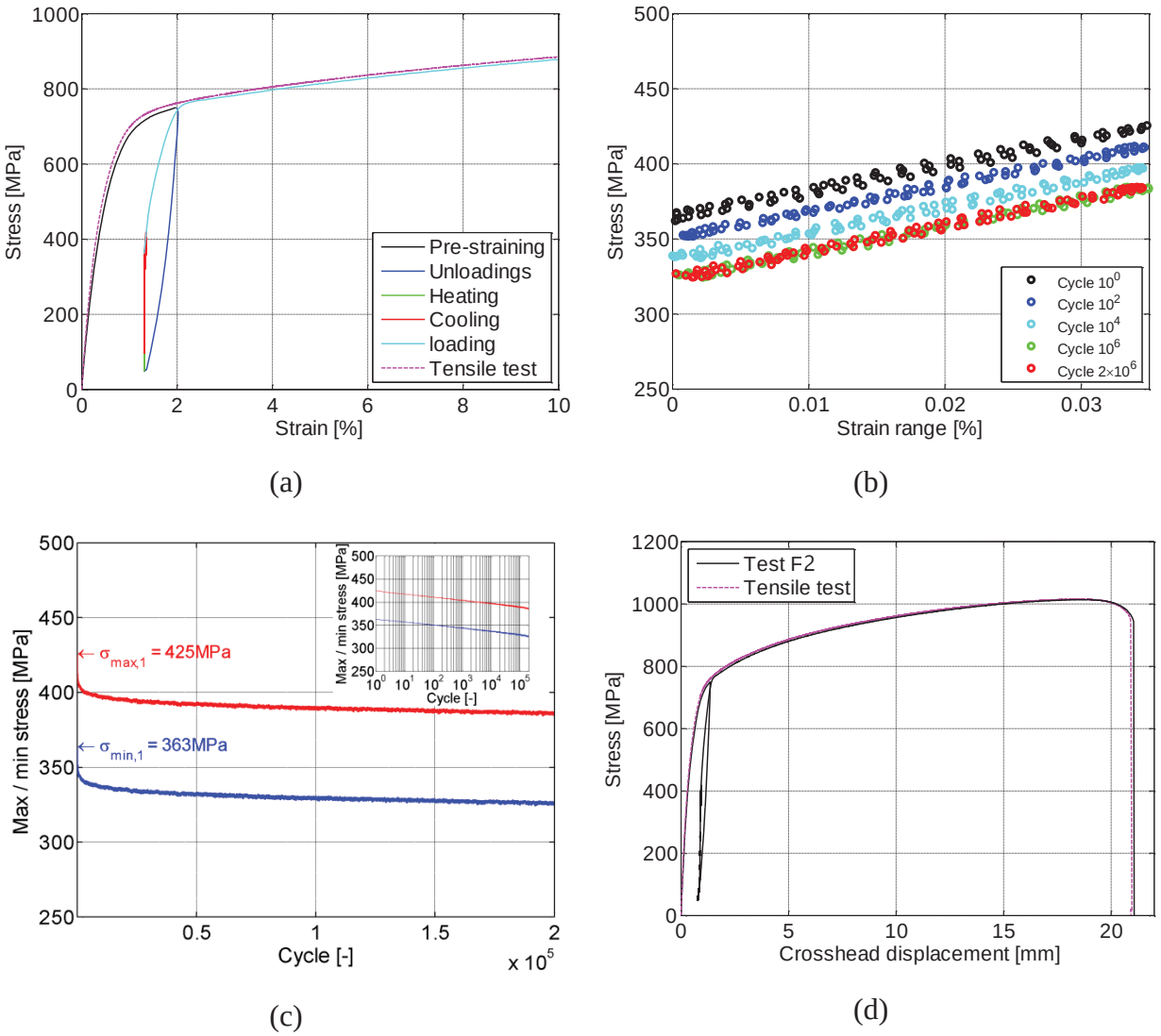

Fig. 9. Specimen F2: (a) the stress-strain response of the SMA during activation, fatigue loading, and the final tensile loading, (b) the enlarged details of the fatigue loading with $\Delta\varepsilon_0$ = 0.035 %, (c) the evolution of stresses versus the number of cycles, and (d) the stress-displacement response during the complete test including the fatigue and final tensile loading.

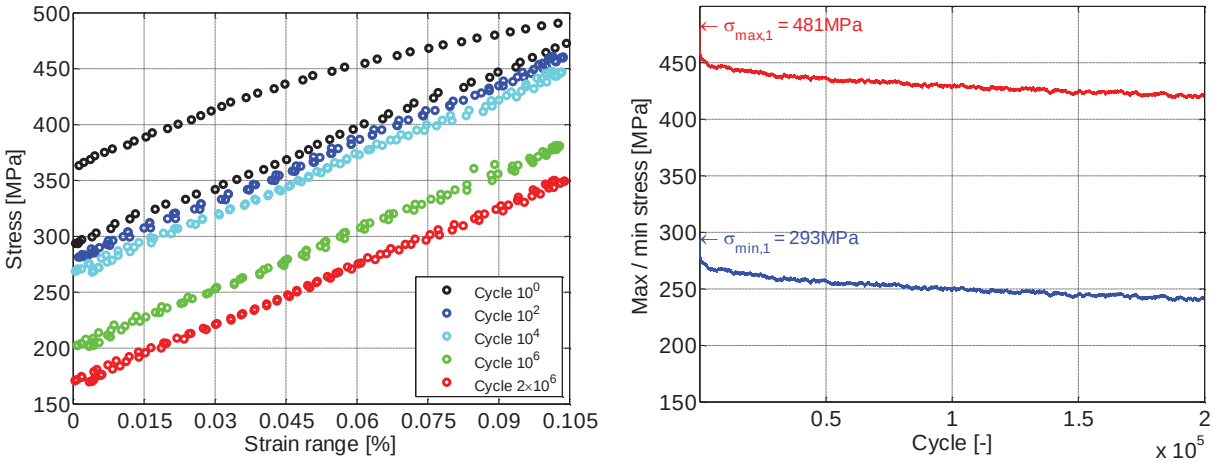

(a) (b)

Fig. 10. Specimen F3: (a) the stress-strain behavior of the activated SMA under fatigue loading with $\Delta\varepsilon_0 = 0.105$ % and (b) the evolution of σ_{max} and σ_{min} versus the number of cycles.

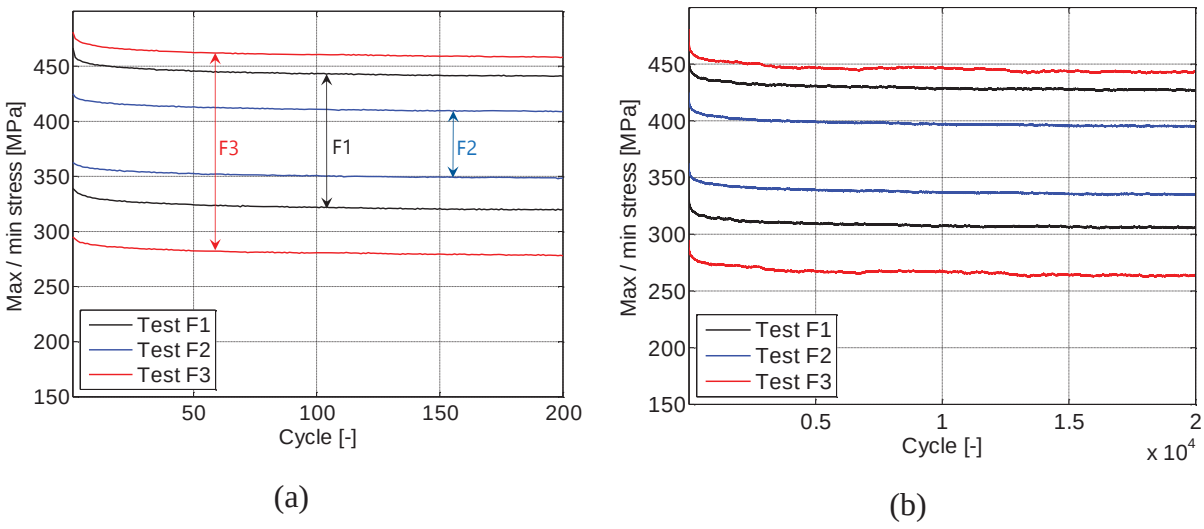

Fig. 11. The evolution of σ_{max} and σ_{min} versus the number of cycles in specimens F1, F2, and F3 for (a) 2×10^2 cycles and (b) 2×10^4 cycles.

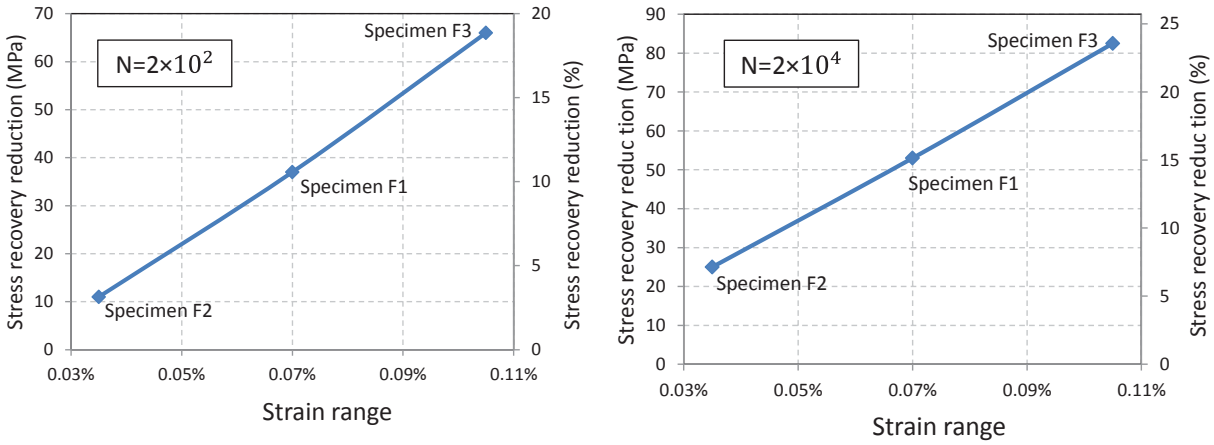

Fig. 12. Reduction in the recovery stress, $\left(\sigma_{min}^{N} - \sigma_{r}^{15m}\right)$ and the loss in percentage compared to the initial recovery stress, $\left[100 \times \left(\sigma_{min}^{N} - \sigma_{r}^{15m}\right) / \sigma_{r}^{15m}\right]$ at (a) 2×10^2 cycles and (b) 2×10^4 cycles.

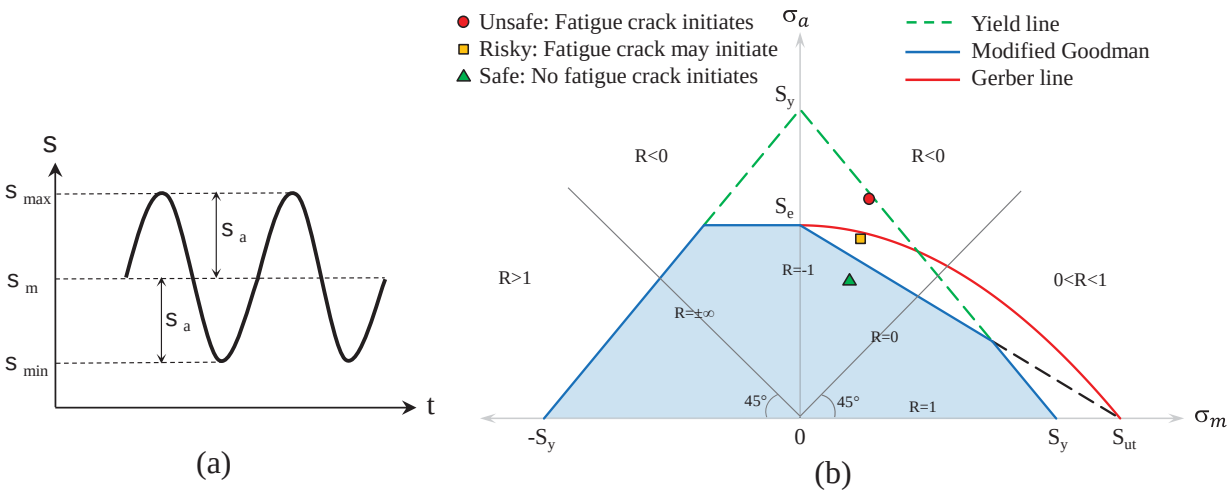

Fig. 13. (a) A typical cyclic stress pattern and (b) the definition of unsafe, risky and safe zones in the CLD approach, according to different fatigue failure criteria for ductile steels [24].

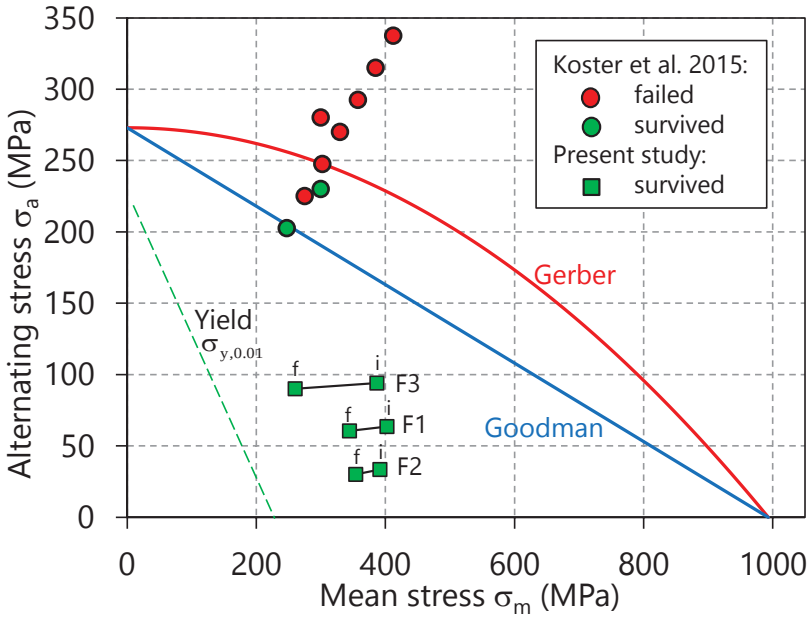

Fig. 14. Results of the fatigue tests on the Fe-SMA analyzed using the CLD methodology.

Table 1. Mechanical properties of the Fe-17Mn-5Si-10Cr-4Ni-1(V,C) SMA, as determined by tensile testing.

E [GPa]	$\sigma_{y,0.01}$ [MPa]	$\sigma_{y,0.2}$ [MPa]	Ultimate tensile strength [MPa]	Elongation at break [%]
173	230	546	1015	54.9

Table 2. Details of the test specimens and their characteristics.

	Stress recovery			Cyclic loading									Final static loading	
Sample ID	σ_r (MPa)	σ_r^{15m} (MPa)	$\Delta\varepsilon_0$ (%)	N_l	Freq. (Hz)	1st cycle			N_l th cycle				Ultimate strength (MPa)	Elongation at break (%)
						σ_{min}^1	σ_{max}^1	$\Delta\sigma^1$	$\sigma_{min}^{N_l}$	$\sigma_{max}^{N_l}$	$\Delta\sigma^{N_l}$			
C1	372	364	0.07	10	0.002	312	434	122	299	422	123		1020	60.6
C2	372	362	0.07	10	10	344	467	123	333	455	122		1025	60.9
F1	368	359	0.07	2×10^6	10	339	466	127	284	405	121		1015	55.4
F2	369	360	0.035	2×10^6	10	358	425	67	324	384	60		1014	56.4
F3	359	345	0.105	2×10^6	10	293	481	188	170	350	180		N/A	N/A

For all specimens:

ε_{pre} = 2 %, σ_0 = 50 MPa, $\varepsilon_r \approx 1.3$ %, and T_h = 160 °C. The strain rate during pre-straining and the final tensile loading was 0.15 % s^{-1}. The heating and cooling rates during activation were maintained at 2 °C/min. All the processes, including pre-straining, unloading, cyclic loading, and final failure were conducted at room temperature (25.5 °C).